A Review of Selective Laser Melting of Aluminum Alloys: Processing, Microstructure, Property and Developing Trends

Article *in* Journal of Materials Science and Technology -Shenyang- · February 2019

DOI: 10.1016/j.jmst.2018.09.004

CITATIONS
80

READS
3,453

5 authors, including:

Jinliang Zhang
Huazhong University of Science and Technology
3 PUBLICATIONS **118** CITATIONS
SEE PROFILE

Bo Song
Huazhong University of Science and Technology
80 PUBLICATIONS **1,779** CITATIONS
SEE PROFILE

Qingsong Wei
Huazhong University of Science and Technology
155 PUBLICATIONS **2,124** CITATIONS
SEE PROFILE

Yusheng Shi
Huazhong University of Science and Technology
351 PUBLICATIONS **4,628** CITATIONS
SEE PROFILE

Journal of Materials Science & Technology 35 (2019) 270–284

Contents lists available at ScienceDirect

Journal of Materials Science & Technology

journal homepage: www.jmst.org

Invited Review

A review of selective laser melting of aluminum alloys: Processing, microstructure, property and developing trends

Jinliang Zhang [a], Bo Song [a,*], Qingsong Wei [a], Dave Bourell [b], Yusheng Shi [a]

[a] State Key Laboratory of Materials Processing and Die & Mould Technology, School of Materials Science and Engineering, Huazhong University of Science and Technology, Wuhan, 430074, China

[b] Dave Bourell Laboratory for Freeform Fabrication, Mechanical Engineering Department, The University of Texas at Austin, Austin, TX, 78712, USA

ARTICLE INFO

Article history:
Received 29 March 2018
Received in revised form 26 April 2018
Accepted 22 May 2018
Available online 12 September 2018

Keywords:
Selective laser melting
Aluminum alloy
Metallurgical defects
Mechanical properties
Heat treatment
Developing trend

ABSTRACT

Selective laser melting (SLM) is an attractive rapid prototyping technology for the fabrication of metallic components with complex structure and high performance. Aluminum alloy, one of the most pervasive structural materials, is well known for high specific strength and good corrosion resistance. But the poor laser formability of aluminum alloy restricts its application. There are problems such as limited processable materials, immature process conditions and metallurgical defects on SLM processing aluminum alloys. Some efforts have been made to solve the above problems. This paper discusses the current research status both related to the scientific understanding and technology applications. The paper begins with a brief introduction of basic concepts of aluminum alloys and technology characterization of laser selective melting. In addition, solidification theory of SLM process and formation mechanism of metallurgical defects are discussed. Then, the current research status of microstructure, properties and heat treatment of SLM processing aluminum alloys is systematically reviewed respectively. Lastly, a future outlook is given at the end of this review paper.

Contents

* Corresponding author.
E-mail address: bosong@hust.edu.cn (B. Song).

https://doi.org/10.1016/j.jmst.2018.09.004
1005-0302/

1. Introduction

Aluminum alloys, the most widely utilized metal structural materials, after iron and steel, have the potential for application and development in the aviation, aerospace, automobile, naval, weapons and power electronics fields due to their low density, high specific strength, easy processing, and good corrosion resistance as well as their excellent electric and thermal conductivity [1–3].

Based on their composition, microstructure and process characteristics, aluminum alloys can be categorized into cast aluminum alloys and wrought aluminum alloys. In general, the alloying element content of cast aluminum alloys is 10%–12%, while that of wrought aluminum alloys is 1%–2% (although, in some cases, it can be as high as 6%–8%) [4]. According to whether the alloy responds to heat treatment by precipitation hardening, aluminum alloys can be further divided into heat treatable and non-heat treatable aluminum alloys, as shown in Fig. 1. The properties of commercial aluminum alloys are shown in Table 1. 2XXX (Al-Cu or Al-Cu-Mg), 6XXX (Al-Mg-Si) and 7XXX (Al-Zn-Mg) series alloys belong to heat treatable alloys, whose strength can be enhanced by various heat treatment processes [4–6]. The 1XXX, 3XXX, 4XXX and 5XXX series alloys are non-heat treatable aluminum alloys that can be strengthened by solid solution and mechanical deformation processes [4,5].

At present, aluminum alloy structural parts are mainly manufactured by traditional methods such as casting, forging, extrusion and powder metallurgy [7]. Although aluminum alloy products made by the above traditional processes have been extensively used, there are still many problems in the process of production and their applications. First, the low cooling rate in the casting processes makes the microstructure coarse, and many defects exist, such as offset defects, shrinkage porosity, slag inclusion and element segregation in cast aluminum alloys, that lower the mechanical properties of the parts [8–10]. Second, the preparation and forming process of high performance aluminum alloy components are separated, which causes a long process chain with limited flexibility. In addition, with the modern industrial developments, the structure and performance requirements of aluminum alloy parts are continuously increasing. For example, to meet the engineering requirements of high thermal conductivity, light weight and high load carrying capacity, the thermal protection system of aerospace vehicle engines commonly uses a lattice or cellular structure. Integral forming of complex structural components not only reduces the time and tooling for fabrication and assembly of small and medium size components but also decreases the weight and stress concentrations normally associated with welding and other joining approaches [11–13]. The production of aluminum alloy parts with diverse structures, high dimensional accuracy and near net shape will be a major research and development objective in the future.

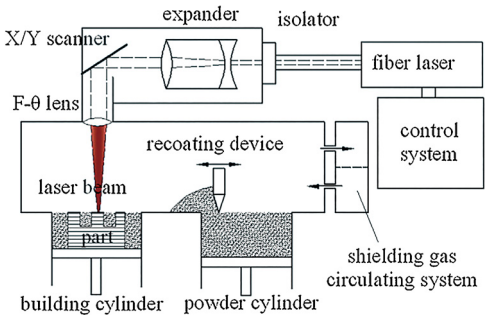

Fig. 2. Schematic diagram of selective laser melting [14].

Selective laser melting (SLM) is considered one of the most promising additive manufacturing (AM) technologies, whose processing schematic diagram is shown in Fig. 2. SLM utilizes a high-energy laser beam to completely melt metal powder in a protective atmosphere along the laser path, and this molten metal rapidly solidifies [14]. By repeating this step and overlapping layer by layer, a three-dimensional component is eventually formed. Such a layerwise approach has a unique advantage in the integrated formation of complex structured and thin-walled components [15,16]. The process of welding and riveting is eliminated, and no mold is needed, thus shortening the design and production times [17]. Recycling the metallic powder increases the feedstock utilization rate and reduces the production cost. In addition, the SLMed parts have excellent quality and performance. The laser interacts with the metallic powder to form a small molten pool on a scale of approximately 100 μm [18]. The cooling rate of the molten pool reaches 10^3-10^8 K/s due to the rapid movement of the laser at 100–1000 mm/s [19]. Such a rapid cooling rate inhibits grain growth and segregation of the alloying elements. Together with the stirring action of Marangoni flow [20] in the molten pool, a fine

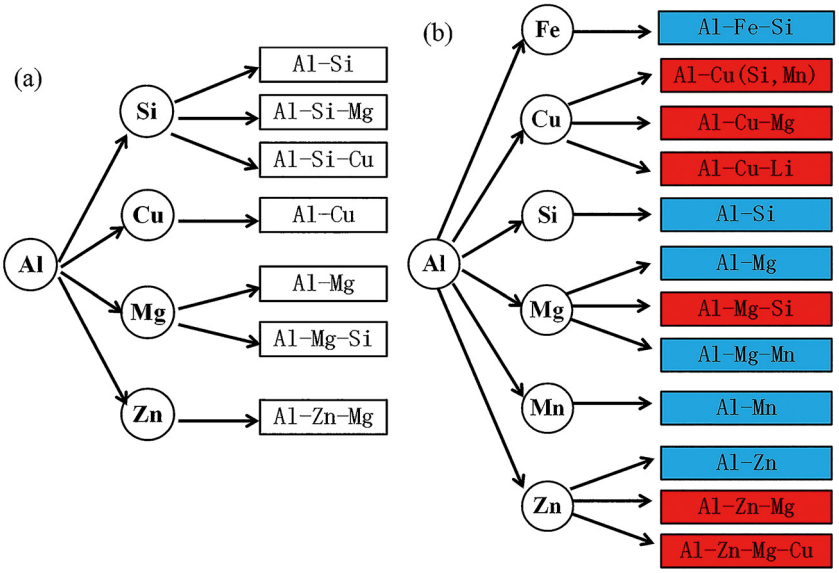

Fig. 1. Classification of cast aluminum alloys and wrought aluminum alloys: (a) cast aluminium alloys. (b) wrought aluminium alloys. Non-heat treatable aluminium alloys are in blue and heat treatable aluminum alloys are in red.

Table 1
Properties of aluminium series alloys.

Series	Types	elements	Performance
1×××	non-heat treatable	Pure Al (≥99.00%)	Low strength, good corrosion resistance and conductivity, easy processing
2×××	heat treatable	Al-Cu/Al-Cu-Mg	Hard-aluminium alloy. High strength, good heat resistance, poor corrosion resistance
3×××	non-heat treatable	Al-Mn	Antirust aluminium alloy. Low strength, cold-working-hardening, good plasticity and weldability
4×××	non-heat treatable	Al-Si	High silicon, low melting point, good weldability, good heat and wear resistance
5×××	non-heat treatable	Al-Mg	High magnesium, good corrosion resistance and weldability
6×××	heat treatable	Al-Mg-Si	Medium strength, good formability, weldability and machinability
7×××	heat treatable	Al-Zn-Mg	Very high strength, cannot be welded, poor corrosion resistance
8×××	/	Other elements	/
9×××	/	Spare alloys	/

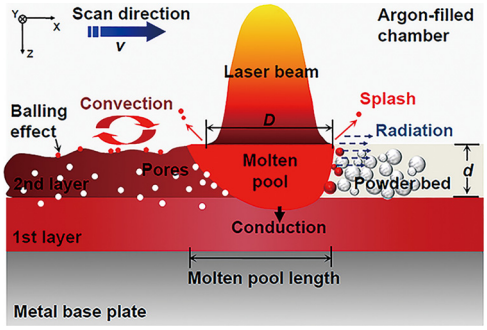

Fig. 3. Diagram of interaction between laser and powder bed [28].

uniform microstructure is formed that significantly improves the strength and toughness. The non-equilibrium solidification process increases the solid solution limit of the alloy elements in the matrix, and new metastable or even amorphous phases may be generated [21–23]. However, the surface quality and dimensional accuracy of the SLMed parts are typically not sufficient to meet the demands of industrial production, so post-treatment processes, such as surface treatment and machining, are required, which increase the production time [24]. On the other hand, the large temperature gradients and complex heat transfer due to the cyclic processing of the laser beam result in the directional growth of grains, so the microstructure and properties of the alloy tend to be anisotropic [25]. The quality of the SLMed parts depends on the selection of the technological parameters, such as the laser power, scanning speed, scanning spacing and layer thickness. These process parameters are influenced by the material characteristics, powder fluidity, particle size/shape/distribution and the type and spot size of the laser [26,27]. The use of improper process parameters may cause balling, pores, cracks and low density.

2. Solidification theory and metallurgical defects of laser selective melting

2.1. Solidification theory of laser selective melting

When the laser contacts the metal powder, a series of complex physical and chemical phenomena occur during the rapid melting and solidification processes, such as the absorption and scattering of laser energy, heat transfer, phase transition and melt flow in the molten pool [28,29], as described in Fig. 3. The thermodynamic and kinetic behavior of the molten pool can be changed by adjusting the processing parameters. The size and shape of the grains and the content and composition of the phases are controlled to obtain the desired microstructure and mechanical properties [30]. Likewise, to explain the microstructure and property evolution laws of SLMed parts, the thermal behavior and solidification theory under the processing conditions must be clearly defined.

As shown in Fig. 4, the growth of grains in fusion welding is considered to be initiated by the epitaxial solidification of the base

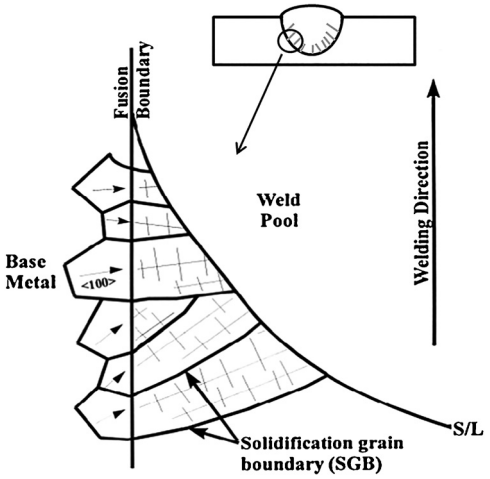

Fig. 4. Epitaxial solidification and competitive growth of welded molten zone [37].

material and growth toward the welding centerline [31,32]. Similarly, under the condition of melt superheating, homogeneous nucleation hardly occurs in the SLM process, and nucleation is always enhanced at the solid-liquid interface between the grain surface of the parent metal and the liquid metal [33,34]. Once crystallization is initiated at the boundary of the molten pool, grains continue to grow toward the interior of the melt in the form of columnar crystals [34]. The crystallization orientation most conducive to the grain growth of aluminum is <001> [35]. Grains growing along the <001> orientation and perpendicular to the isotherms of the molten pool boundary, where the heat dissipates fastest, can keep growing to the interior of the molten pool. However, grains growing along the <001> orientation but in the direction of the boundary isotherm are inhibited and grow only a short distance [36,37]. This phenomenon is known as preferential growth.

The cooling and solidification mode of the molten pool mainly depends on the laser energy density and the interaction period of the laser and the material [38]. The temperature gradient is given as $G=\mathrm{d}T/\mathrm{d}x$, the solidification rate is given as $R=\mathrm{d}x/\mathrm{d}t$, and the cooling rate is given as $\mathrm{d}T/\mathrm{d}t = G{\cdot}R$. A higher cooling rate $G{\cdot}R$ can improve the undercooling of the melt and refine the grains [39,40]. When the ratio of the temperature gradient and the solidification rate G/R increases, the crystal morphology changes from dendritic to cellular and finally to planar crystal [19,41]. The scale and the type of microstructure are controlled by $G{\cdot}R$ and G/R, respectively.

The microstructure undergoes a morphological evolution from planar to cellular, cellular dendrite and an equiaxed crystal with the successive decreases of $G{\cdot}R$ [19,41]. Therefore, the solidification structure often has a variety of grain types in the SLM solidification process. As shown in Fig. 5, when the temperature gradient G_1 at the front of the solid-liquid interface is high, the actual temperature in the liquid phase is higher than the liquidus temperature

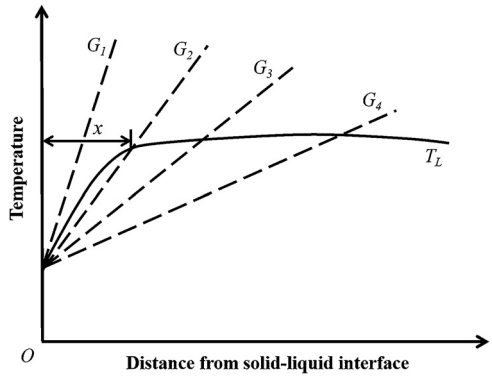

Fig. 5. Conditions of constitutional supercooling.

T_L, and a constitutional supercooling zone will not appear. The nuclei growing forward are remelted by the superheated liquid metal, and the solidification interface is smooth with no solute segregation in the grains. Thus, a planar microstructure is formed. On the condition that the temperature gradient G_2 of the liquid phase becomes lower, a constitutional supercooling zone may be formed. Many parallel small grains form at the solidification interface and protrude into the supercooled liquid due to the unstable state of the planar crystal interface. The solute is expelled toward the lateral subgrain boundaries, and the liquidus temperature of the subgrain boundary decreases. As a result, a bundle of parallel prismatic substructures with hexagonal cross sections are formed in the grain. In this case, a cellular grain structure is formed. If the temperature gradient G_3 further decreases, the cellular crystalline microstructure can penetrate deep into the interior of the liquid for a longer distance, and constitutional supercooling also occurs in the transverse direction. Secondary dendrites may appear on the primary dendrites, which is a characteristic of cellular dendrites. If the temperature gradient G_4 continues to decrease, the constitutional supercooling zone further expands, and dendritic grains are formed. The contact surface of the secondary dendrites is the boundary of the grains. The larger the solidification rate is, the smaller the dendrite spacing is [42]. At the same time, nucleation could also occur in the liquid to produce new grains, which finally grow into equiaxed grains. Because of the Gaussian distribution of the laser energy, the temperature gradient and crystallization rate, as well as the distribution of the undercooling, are different in the different zones of the molten pool [43]. Therefore, various grain morphologies might be expected to appear in the solidified microstructure. At the molten pool boundary, it is hard to induce constitutional supercooling resulting from the large temperature gradient and slow solidification velocity, so planar grain formation is most common. With the grains growing toward the melt pool center, the temperature gradients decrease, and the grain growth rate, mass fraction of solute and constitutional supercooling zone increase gradually. Correspondingly, the substructures in the columnar grains are cellular grains, cellular dendritic grains and dendritic grains, successively. When the grains grow toward the center of the molten pool, equiaxed grains may form eventually [23]. The above theory has been confirmed by the literature [44], as shown in Fig. 6.

The extent of the grain refinement depends on the cooling rate $G{\cdot}R$. A higher cooling rate in the core of the molten pool results in finer grains than those at the edge of the molten pool [45], which can also be observed in Fig. 6. Therefore, the microstructure of SLMed alloys can be controlled by adjusting the technological parameters. A low laser scanning velocity and a high laser power can increase the laser energy density and the interaction time between the laser and material, thus increasing the solidification

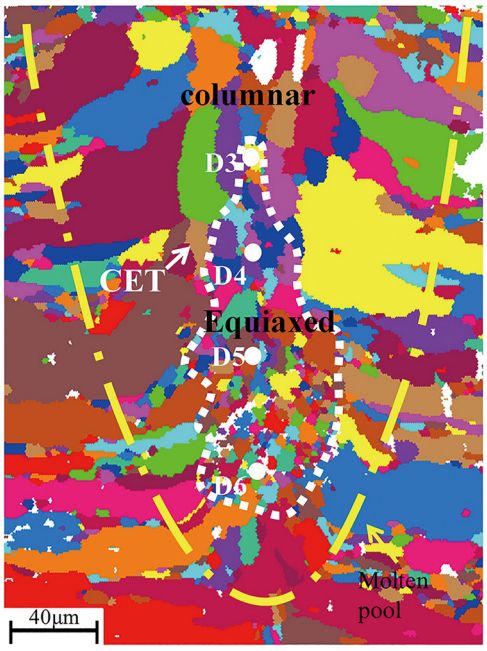

Fig. 6. Grain map measured by electron backscattered diffraction technology [44].

time and the temperatures of the melt and base material, which induces low temperature gradient and cooling rate of the solidification interface to cause a coarse microstructure [43,46]. In contrast, a low laser power and a high scanning velocity inhibit the growth of grains. The cooling rate also has an important influence on the dendrite arm spacing size [45]. The relationship between the dendrite arm size and the cooling rate is revealed as:

$$\lambda = c \cdot T^{-n} \quad (1)$$

where c is the constant of the alloy and n is the rate exponent. This equation indicates that the dendrite size decreases with increasing cooling rate. Additionally, the sub-boundary formation can be affected by a fast cooling rate. As a result, the surface always has a higher hardness and a greater wear resistance value due to the finer precipitate phase particles being evenly distributed, finer dendrites and the occurrence of sub-boundaries compared with the core area.

2.2. Formation mechanism and control methods of metallurgical defects

2.2.1. Balling

According to the minimum principle of surface energy, a liquid metal will shrink into a spherical shape driven by surface tension when it is in poor contact with a substrate. This is termed the balling phenomenon [47]. The balling phenomenon results in a rough surface on the solidified layer accompanied by a large number of pores, which reduces the density and quality of the parts and may even damage the powder roller or scraper, which fails the process [48,49].

Generally, the balling phenomenon can be attributed to the poor wettability and droplet splashing during processing. As shown in Fig. 7, the molten pool can be divided into an upper part consisting of the molten powder and a lower part consisting of the molten substrate material [50]. The gas-liquid interface of the upper molten pool tends to promote the balling phenomenon, while the lower melt pool hinders the balling trend of the upper part. If there is enough melt in the lower molten pool, the balling tendency of the upper melt pool will be completely suppressed [50,51]. Therefore, a high energy density can form sufficient liquid metal and helps to mitigate the balling phenomenon. Moreover, a high tempera-

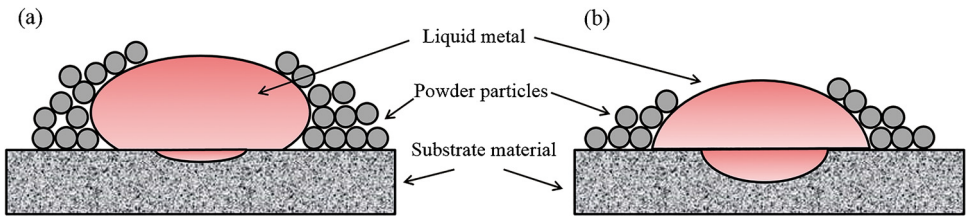

Fig. 7. Schematic diagram of balling phenomenon. (a) Less molten substrate material. (b) More molten substrate material.

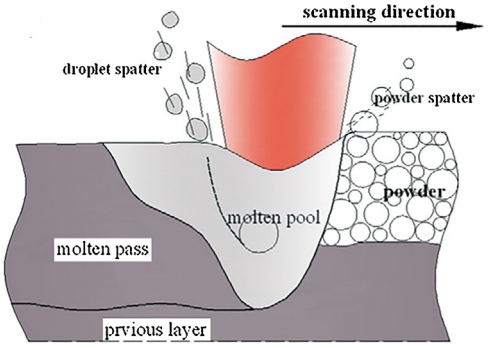

Fig. 8. Schematic diagram of droplet splash during SLM [14].

ture can lead to low viscosity and good fluidity of the liquid metal, thus enhancing the wettability of the melt and the solidified layers. However, if the laser energy is too high, excessive liquid metal will lead not only to balling but also to deformation of the parts due to residual stress formation [52,53].

Excessive temperature will also cause evaporation of the material. As shown in Fig. 8, the rapid formation of a gaseous phase produces a large recoil pressure in the molten pool, causing some melt to escape in the form of a metal jet [54]. The metal jet is broken up into droplets by metallic vapor and the laser beam, finally forming metal balls. In addition, due to the influence of the metal vapor, the unmelted metal powder around the molten pool may be dispersed and splashed sideways [14].

Laser remelting may provide a means for the metal balls to rewet the substrate, reducing the balling phenomenon, but it simultaneously increases the manufacturing time [48,55,56]. Substrate preheating can improve the wettability between the melt and substrate and thus restrain the shrinkage effect during solidification, resulting in good metallurgical bonding [57]. However, when the preheating temperature is too high, some powder particles may form agglomerates attached to the molten pool, causing an even more severe balling phenomenon [58]. The preheating temperature of aluminum alloys is commonly within the range of 50–200 °C.

2.2.2. Porosity

The pores in the SLMed parts are divided into three types: fusion errors, gas pores and shrinkage pores [59–61]. Fusion errors are attributed to insufficient laser energy density, which causes incomplete remelting of the last solidified layer and a poor metallurgical bond [62]. These pores are irregularly shaped and are common at the interfaces of the layers. Their size and number are greatly affected by the processing parameters. The gas entrapped in the gaps of powder particles in the powder mass contributes to the formation of fusion errors [63]. When laser scanning is progressing, the gas escapes and thereby results in unstable scanning paths. With the formation of these cavities, the fluid force in the molten pool tends to balance with the vapor pressure in the cavity, causing the liquid metal to collapse and form periodic pores [64–66]. Shrinkage porosity is mainly attributed to an insufficient supply of liquid metal during the solidification process [62,67]. Since bubbles always tend to exist in the minimum surface energy state, the gas pores are generally spherical and fine [63,68,69]. The main source of this type of porosity is the inert gas in the protective atmosphere involved in the molten pool that is incorporated into the part via surface turbulence, the gas in the powder particle gaps, or the vapor of the low melting compounds in the alloy that fails to escape from the molten pool [63,70].

Gu et al. [71] studied the effect of the shielding gas on the molten pool dynamics, the evaporated material velocity field and the resultant surface morphology by numerical simulations, as shown in Fig. 9. It was found that when a He protective atmosphere was used, the velocity field vector of the evaporated metal is in a horizontal or downward direction, and the nonuniform recoil pressure generated on the surface of the molten pool results in the occurrence of keyholing. When an Ar protective atmosphere is used, the upward velocity field vectors make it difficult to trap gases, so a uniform recoil pressure and a stable condition of the molten pool are formed, which leads to a relatively flat surface morphology. When a N_2 protective atmosphere is applied, the metal vapor tends to flow toward the laser-powder interaction region, resulting in material stacking and poor surface quality. In the actual SLM processing of AlSi12, the defects of the samples are fewer in atmospheres of Ar and N_2. In an atmosphere of He, however, there are some pore clusters in the microstructure in local areas. Because these areas are relatively small, the overall density values of the SLMed samples are not significantly affected, but lower mechanical properties are produced for the SLMed samples, especially the ductility [72]. The porosity of the fracture morphology under a He atmosphere was significantly higher than those under Ar and N_2. Cracks will first form and expand rapidly in the pore concentration areas, resulting in the fracture of the material.

In the previous section, it has been mentioned that if the balling phenomenon is severe on a certain layer, it will inevitably lead to a 'ripple effect' such that large amounts of balling and porosity occur on the next layer. This results in the formation of metallurgical defects and low density in the final part. Therefore, strategies to diminish balling by adjusting the process parameters, substrate preheating and remelting are equally applicable for reducing the porosity. Sufficient liquid metal supply and long molten pool lifetime enhance complete filling of the pores during SLM processing. For aluminum alloys, the water absorption of aluminum powder is strong, and the solubility values of hydrogen in solid and liquid aluminum are different [73,74]. The powder material should therefore be sufficiently dried before processing to prevent the formation of hydrogen porosity during rapid solidification.

2.2.3. Residual stress and cracking

Rapid melting and solidification during SLM manufacturing processing lead to a higher cooling rate and temperature gradient in the molten pool [19]. Owing to the continuous thermal cycling and complex physical/chemical reactions, an inhomogeneous heat distribution leads to the thermal expansion and contraction of the solidified structure [29]. Therefore, the SLM process is inevitably accompanied by high residual stress levels. High residual stress zones formed around the molten pool may lead to cracking, delami-

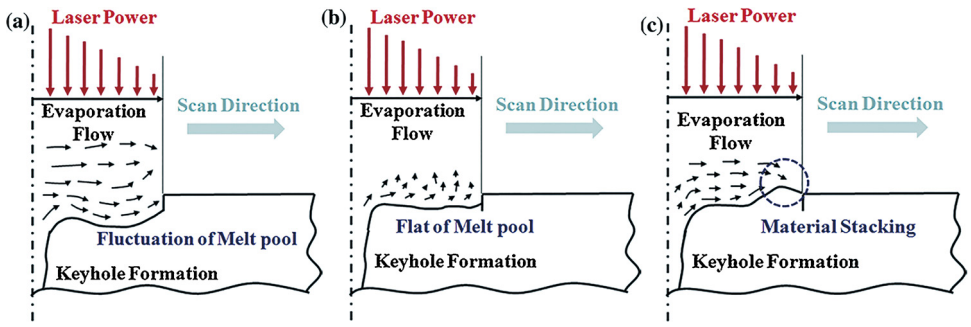

Fig. 9. Diagram of velocity field of evaporated metal. (a) He. (b) Ar. (c) N_2 [71].

nation, fatigue failure and thermal deformation [75,76]. As a result, the dimensional accuracy and mechanical properties of the parts will be significantly affected [24]. Crack formation in aluminum alloys is even aggravated due to its high thermal conductivity, wide solidification temperature range, high thermal expansion coefficient and severe solidification shrinkage [77].

The stresses formed in the SLM process are mainly classified into thermal stresses and structural stresses [78]. The thermal stress is caused by the uneven heating of the laser and the resultant different amounts of thermal expansion and shrinkage deformation between the regions near to and away from the molten pool [79,80]. When phase transformation occurs in the SLM process, the material will undergo volume expansions and contractions arising from the different specific volume of phases, thereby resulting in structural stresses [81]. Thermal stress is the primary cause of crack initiation in SLM [82]. When the stresses inside the part exceed its yield strength, either plastic deformation occurs, possibly resulting in part distortion, or cracks may form to relieve the stress [83]. Considering the complexity of the SLM process and the difficulty of experimental measurement, finite element simulation methods are often used to predict the distribution and evolution of residual stress.

Similar to the welding of aluminum alloys, cracking in SLM can be divided into liquation cracking and solidification cracking [84]. Liquation cracks often occur in alloys with high amounts of alloying elements [85]. These alloys will precipitate many low melting point eutectics in the heat affected zone and overlapping regions between layers that will be remelted under the peak temperature of the thermal cycle [86]. Thus, cracking occurs under tensile stress. At present, there have been few studies of the formation mechanism and influencing factors of liquation cracks produced by SLM in various kinds of metallic materials. In the final stage of solidification, hot cracking caused by the residual liquid film between the crystals in the mushy zones is termed solidification cracking [87]. Solidification cracking is closely related to the range of the solidification temperature and the content of liquid during solidification [88,89]. Ductility-dip cracking (DDC) is one of the key mechanisms of crack formation during the SLM process and often occurs at a moderate temperature where the ductility and tensile properties are relatively low [90]. The DDC mechanism usually induces the formation of intergranular cracks, and crack initiation is more likely to occur in the presence of high angle grain boundaries [31,91,92]. Because the solidification strain is directly related to the solidification temperature range where the ductility and tensile properties are lower, alloys with a wide temperature range of solidification are more likely to exhibit crack initiation [93,94]. Regarding the SLM process, owing to the lack of diffusion in the non-equilibrium rapid solidification process, the solidus and liquidus temperatures decrease, and the temperature range of solidification becomes wider [84]. The residual liquid in the mushy zone along the grain boundaries becomes film-like in shape, which results in strain concentration [95]. Crack initiation is more likely to occur. The addition of alloying elements, which are beneficial to narrowing the solidification temperature range, can modify the composition of the molten pool and prevent cracks [96]. For example, 5XXX series aluminum alloys have a lower cracking tendency than the 2XXX, 6XXX and 7XXX series aluminum alloys in laser processing.

Shiomil et al. [79] found that laser remelting and substrate preheating can effectively reduce the residual stress by 55% and 40%, respectively, during processing due to the reduction of the cooling rate. The formation of cracks also depends on the choice of process parameters. Only when the energy density is exactly the optimum value or within the optimum range can a crack-free, dense SLMed part be manufactured. When the energy density is low, a disordered solidification front of liquid metal and severe balling will lead to crack formation [67]. To diminish residual stress and crack formation, sufficient liquid phase should be ensured to backfill the cracks and take up the solidification strain [97]. At extremely high energy density values, low liquid viscosity and long liquid lifetime will result in an increase of thermal stress [98]. Excessively rapid cooling rates should also be avoided when setting the process parameters. Too high a cooling rate will accelerate the development of thermal strain and will increase the stress gradient, thus enhancing the crack initiation rate [78]. Furthermore, excessively rapid cooling also reduces the time available for the liquid to refill and heal the cracks.

2.2.4. Oxidation

Although parts are processed under a protective atmosphere, there is still approximately 0.1% oxygen in the real production process due to air filling in the gaps between the powder particles. Similar to the casting process, oxide inclusions in SLM mainly come from two sources. One is due to the partial oxidation of the powder raw material. The other arises from oxygen entrapped from the atmosphere by the surface turbulent flow of the molten pool [63,70]. Al_2O_3 formed during SLM processing of aluminum alloys hinders the fusion of the powder particles, lowers the metallurgical bonding effect between the solidified layers and scanning paths, aggravates the balling phenomenon and reduces the densification of the alloy [99,100]. Oxide inclusions often induce crack initiation, lowering the mechanical properties of the parts [99,101].

Louvis et al. [102] used a NaOH solution to deeply corrode 6061 aluminum alloy, revealing the oxidation mechanism and oxide film morphology of the SLMed aluminum alloy. As shown in Fig. 10(a) and (b), oxide films can form on all sides of the molten pool in the process of laser processing. The oxide films on the upper surface evaporate and form fumes escaping from the molten pool under the laser beam. The oxide films on the lower side of the molten pool are broken up by the stirring action of the Marangoni flow. Thus, the "walls" of oxide film around the weld pool are retained, and oxide films with a network distribution are observed after deep corrosion, as shown in Fig. 10(c). The existence of these oxide films reduces the

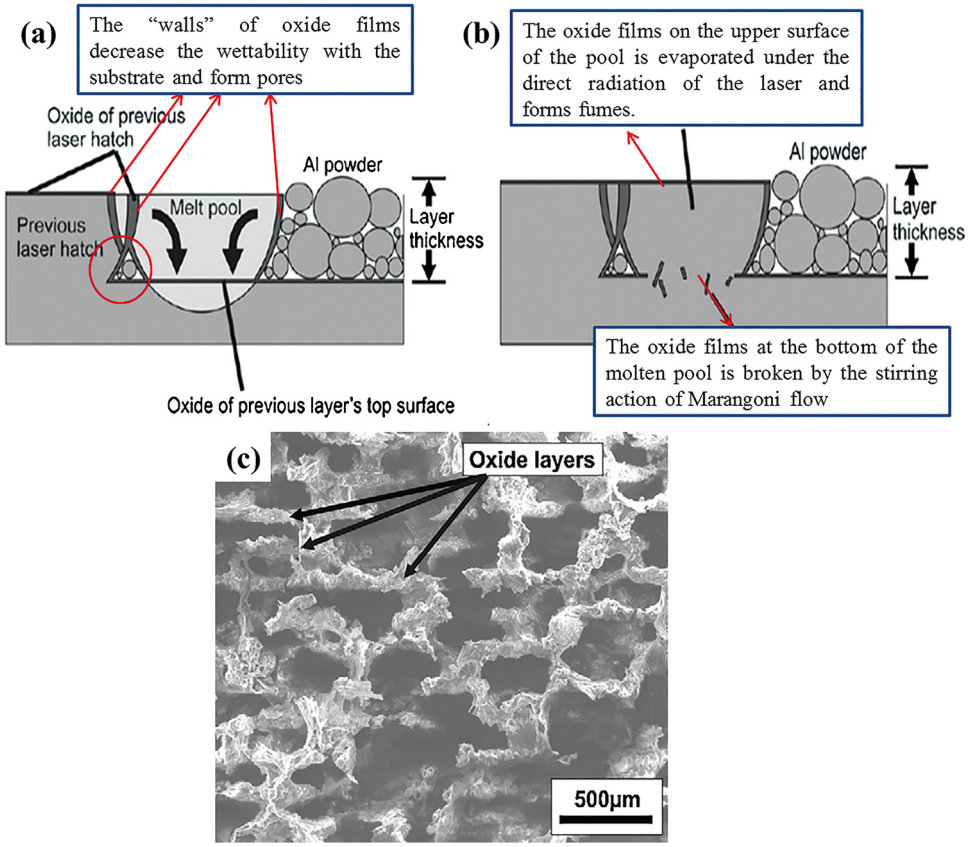

Fig. 10. Formation mechanism and morphology of oxide film [102]. (a) Oxide disruption of the molten pool. (b) The walls of oxide films. (c) SEM image of oxide films after deep corrosion.

wettability of the melt and substrate, and the overlapping portions of the adjacent tracks form closed or semi-closed pores, in which some melt or unmelted powder particles are trapped.

To reduce oxidation in SLM, besides maintaining sufficiently low oxygen partial pressure, the metal powder must be clean and dry. Under laser action, moisture on the powder surface can be decomposed into H_2 to produce hydrogen porosity and oxygen combined with aluminum melt to form alumina [103].

2.2.5. *Loss of alloying elements*

In additive manufacturing using laser or electron beam melting technologies, the high superheat of the molten pool and evaporation losses of alloying elements will inevitably lead to the deviation of the original alloy composition and reduction of performance [104–106].

Serious losses and uneven distribution of Al in as-SLMed TiAl samples have been observed, and the corresponding Al loss of single tracks varies from 5.73 to 0.32 at% [53]. Significant Al losses and segregation have also been reported in the literature in the selective electron beam melting (SEBM) manufacturing process [104,105]. The loss of tin is observed on the fracture surfaces of SLMed Cu-4Sn specimens [107]. These samples simultaneously display step surfaces and dimples, thus implying that the production of brittle cleavage fracture and ductile fracture can be ascribed to the segregation of tin in the sample. The dissipation of elemental Mg or Zn from an aluminum alloy not only reduces the precipitation strengthening effect and mechanical properties but also decreases the stability of the scanning tracks [108]. Therefore, the loss of alloying elements is also an important reference criterion for the optimization of the process parameters. In addition, the loss of alloying elements may cause a reduction of the amount of non-spontaneously nucleated particles in the molten pool, which is an important cause for the development of columnar grains [36].

The energy density is identified as a key parameter affecting vaporization. High loss of alloying elements usually occurs at high energy density due to overheating and evaporation of volatile elements [53,105]. However, the chemical composition variation within an SLMed part is a function of the evaporation rate of the elements and the volume of the molten pool. Although the evaporation rate of the elements increases with the energy density, the small volume of liquid metal causes a high specific surface area of the molten pool, so the evaporation rate of alloying elements is also enhanced at too low an energy density level [108]. Therefore, the combination of moderate laser power with a high scanning speed is the key to avoiding the evaporation of low-melting-point, low-vapor-pressure elements.

3. Solidification theory and metallurgical defects of laser selective melting

Most research on SLM-fabricated metals focuses on ferrous-, nickel- and titanium-based alloys [49,109,110]. With the development of research and technology, the SLM process of aluminum, copper- and magnesium-based materials has begun to mature [107,111–113]. Compared with iron-, nickel- and titanium-based alloys, the difficulties of processing aluminum alloys by SLM are as follows [84,102,114].

(1) The poor fluidity of aluminum alloy powder induces the formation of agglomeration when spreading the powder, which results in an uneven thickness of the powder layers and affects layer quality.

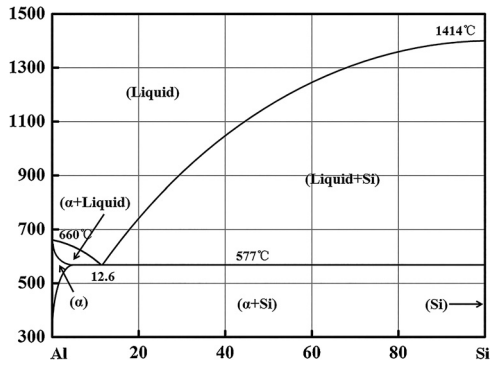

Fig. 11. Al-Si phase diagram.

(2) The laser reflectivity of aluminum reaches 91%. The thermal conductivity of aluminum is 237 W/(mK), which is eleven times the value for Ti and five times the value for Fe. A higher cooling rate leads to crack initiation. Less heat accumulation during processing is more likely to cause the formation of metallurgical defects such as pores and cracks. Therefore, a higher laser power is required to form dense parts, so higher power demands on the equipment are required.
(3) Aluminum oxidizes easily. The existence of oxide films will induce surface passivation of the molten pool and promote the formation of metallurgical defects, which results in strict requirements for the vacuum or oxygen partial pressure of the processing environment.
(4) The moisture absorption of aluminum alloy powder is strong, and the solubility values of hydrogen in solid and liquid aluminum are very different. Thus, hydrogen porosity is easily produced when the melt solidifies rapidly.
(5) The high thermal expansion coefficient and wide solidification temperature range of aluminum may generate a large amount of residual stress during rapid solidification, which causes the parts to crack and deform.
(6) Aluminum alloys often contain Mg and other low melting point compounds. The fluctuation of alloy composition and crack formation occur easily during laser cycling.

At present, SLM-fabricated aluminum alloys are mostly casting grade Al-Si alloys, especially AlSi10Mg and Al-Si12, whose castability and weldability are relative good. The demand for more aluminum alloys and the development of SLM technology have resulted in studies of Al-Mg, Al-Cu-Mg, Al-Si-Mg, zirconium-modified aluminum alloys and other wrought aluminum alloys. In this chapter, the research progress on the microstructure and properties of various SLMed aluminum alloys is summarized.

3.1. Al-Si series alloys

Al-Si casting alloys are widely used in the automotive and power transmission industries [115]. Fig. 11 shows that the compositions of AlSi10Mg and AlSi12 are near the eutectic points, where the melting point is lower and solidification temperature range is narrower. Therefore, near-eutectic Al-Si cast alloys have good casting properties and less shrinkage porosity, so they are more suitable for SLM processing [116].

3.1.1. Microstructure characteristics of SLMed Al-Si alloys

There are two characteristic temperatures in the melting and solidification process of Al-Si alloys: the dissolution temperature (T_d) and the branching temperature (T_b) [117,118]. When the temperature is below T_d, the liquid phase contains Al and Si-rich particles separated from the powder. When the temperature is above T_d, these particles begin to melt. At temperatures above T_b, the molten Al and Si are uniformly distributed in the liquid phase. T_d (AlSi10Mg: 1020 ± 30 °C, AlSi12: 1080 ± 30 °C) and T_b (AlSi10Mg: 1170 + 30 °C, AlSi12: 1090 ± 30 °C) are both significantly higher than the eutectic temperature of the Al-Si alloy (557 °C) [119,120]. In the molten pool, the temperature of most areas is between T_d and T_b, so most of the melt is in an overheated state, which leads to an uneven distribution of Al and Si. In addition, the short interaction time between the laser and material, vibration of the liquid phase and capillary action also contribute to inhomogeneity in the microstructure [120]. The Al-Si phase diagram shows that the solidification of AlSi10Mg undergoes a phase transition reaction $L \rightarrow L+\alpha$ and a eutectic reaction $L \rightarrow \alpha+Si$ successively, and the solid solubility of Si in the Al matrix reaches 8.89 at.% during SLM processing [117]. During solidification, Si particles whose melting point is higher are first heterogeneously nucleated in the melt pool. With decreasing temperature, α-Al nucleates and grows in the depleted region around the silicon particles. The continuous solidification of α-Al leads to a gradual increase in the concentration of Si in the residual liquid phase, which makes the liquid composition gradually move toward the eutectic range, forming the Al-Si eutectic [121–123]. A large temperature gradient in the molten pool leads to a great undercooling of the melt, resulting in the fiber morphology of the Si crystal. Therefore, the microstructure has a grid-like pattern of fibrous Si embedded in a supersaturated Al matrix in the SLMed AlSi10Mg alloy. Fig. 12(a) and (b) present a network of ultrafine cellular structures with an average diameter of ~500 nm, which is often observed in studies of SLMed Al-Si alloys [124,125]. From the inverse polar figure obtained by Electron Backscattered Diffraction (Fig. 12(c)), the average grain size is revealed as ~10 μm, which is a magnitude larger than the cell size [125]. The Si phase of cast Al-Si alloy is rod-like or acicular, and the microstructure is coarser, as shown in Fig. 12(d). Compared to the Al-Si alloys made by conventional methods, the ultrafine eutectic microstructure formed by SLM has better mechanical properties.

3.1.2. Mechanical properties of SLMed Al-Si alloys

The microstructure of the Al-Si alloy, such as the size and morphology of the Si particles and the intermetallic compounds, dictates the mechanical properties of the parts [126]. At present, studies on the mechanical properties of SLMed aluminum alloys mostly involve hardness and tensile properties, which are summarized in Table 2. The Vickers hardness of SLMed AlSi10Mg is approximately 130–150 HV, which is double that of the EN 1706 die casting alloy [127]. Residual stresses are not always detrimental to the manufacturing process of SLM. They can also improve the hardness of a component if at a reasonable level [80,128]. This is another reason for the increase in hardness of SLM specimens. The increase of hardness also improves the wear resistance of SLM parts. The hypereutectic AlSi50 aluminum alloy has a hardness value of 188 HV. As a reinforcement material in the sliding process, the primary Si improves the friction and wear properties of the alloy [129]. However, with such a high content of Si, macro-segregation of the primary Si is observed due to Marangoni convection and the temperature difference between the interior and exterior of the molten pool [130,131].

Owing to the fine grain strengthening and solid solution strengthening associated with SLM processing, the yield strength (YS) and ultimate tensile strength (UTS) of SLMed specimens are superior to those of Al-Si alloys fabricated by conventional powder metallurgy [125] and casting methods [132,136], but the plasticity is reduced. Similar ultimate tensile and yield strengths were obtained from different research groups in both cases (UTS = 380–450 MPa; YS = 250–350 MPa). The differences in mechanical properties are mainly attributed to the diverse SLM process conditions, which lead to some deviations in the densities and

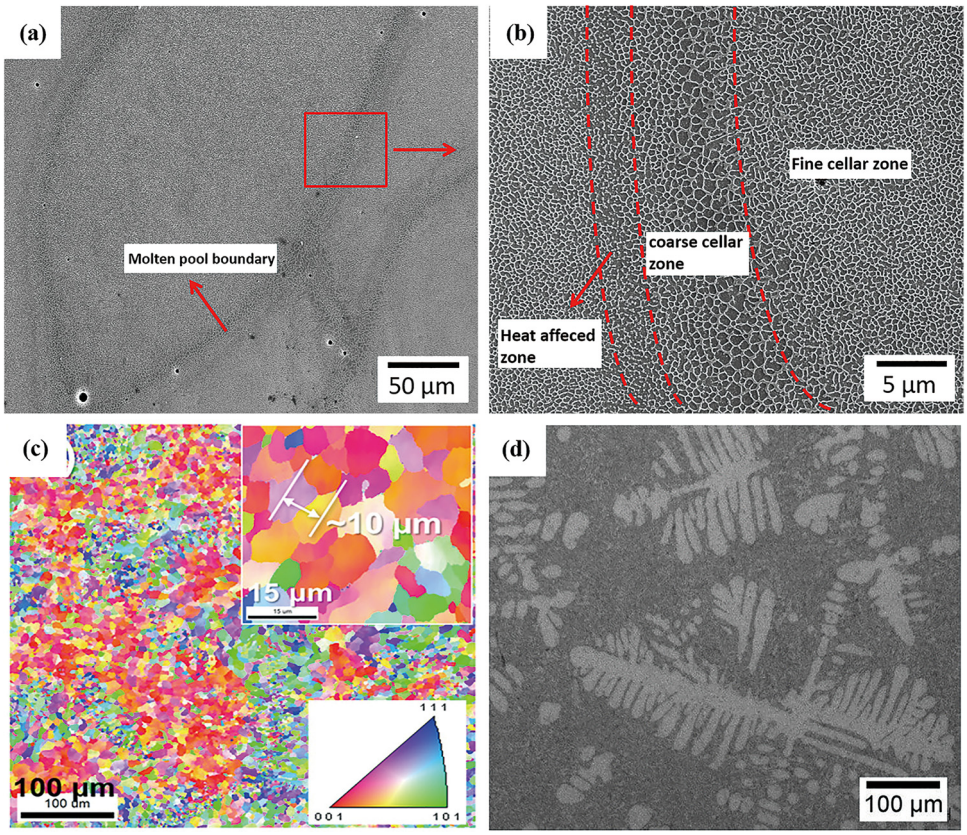

Fig. 12. (a) SLMed Al-Si alloy microstructure at low magnification. (b) SLMed Al-Si alloy microstructure at high magnification. (c) Inverse polar figure obtained by EBSD [125]. (d) Casting Al-Si alloy microstructure [124].

Table 2
Mechanical properties of SLMed Al-Si alloys from different literatures.

Material	Condition	Hardness(HV)	Yield strength(MPa)	Ultimate Tensile Strength(MPa)	Elongation(%)	Reference
AlSi10Mg	As-SLMed	—	~270	~375	~4	[132]
	As-SLMed	~136	–	~396	~3.5	[133]
	As-SLMed	139-146		~360	~6	[134]
	As-SLMed	~133	~322	~434	~5.3	[117]
	SLM + solution at 450 °C	~90	~196	~282	~13.4	[117]
	SLM++solution at 550 °C	~60	~90	~168	~23.7	[117]
	SLM + T6	~78	–	~187	~19.5	[117]
	As-SLMed	125	~268	~333	~1.4	[135]
	SLM + T6	~103	~239	~292	~3.9	[135]
	As-SLMed		~311	~391	~7.2	[136]
	As-SLMed		~300	~455	~5.4	[136]
	As-SLMed		~255	~377	~1.2	[137]
	SLM + annealing		~158	~256	~9.9	[137]
	SLM + T6		~210	~284	~4.9	[137]
AlSi12	SLM + solution		~110	~190	~25	[118]
	As-SLMed		~260	~380	~3	[138]
	SLM + annealing		~95	~140	~15	[138]
AlSi9Mg	As-SLMed		328	379	~8.1	[138]
AlSi7Mg0.3	As-SLMed		~200	~400	12-17	[139]
AlSiMg0.75	As-SLMed	~150	354.9	427.7	2.54	[140]
	SLM + annealing	~110	275.4	360.2	4.57	[140]

microstructures of the samples, such as imperfections, texture and cell size [141].

The fatigue property is a critical attribute for reliable applications in functional industrial components. However, studies on the fatigue properties of SLMed aluminum alloys are much fewer than those on their static properties. Brandl et al. [142] investigated the effect of the platform temperature, build direction and heat treatment on the fatigue strength of AlSi01Mg. Peak hardening has the most considerable and building direction the least significant impact on the fatigue resistance. By choosing the best combination of parameters, a fatigue limit of ~200 MPa (with no substrate heating, 0° orientation and T6 heat treatment) could be attained. The combination of 300 °C platform heating and peak hardening is a valuable approach to increase the fatigue resistance (and the static tensile strength) and neutralize the differences in fatigue life for the 0°, 45°, and 90° directions. The breakthrough cracks always start at the surface or subsurface (pores, non-melted spots), which has also been reported for SLMed AlSi12 alloy [143], Ti6Al4V [144,145] and 316 L stainless steel [146].

Table 3
Mechanical properties of AlSi12 via SLM and casting in literature [124].

Test condition	YS (MPa)	UTS(MPa)	e_f (%)	K_q(MPa$\sqrt{m}$)	ΔK_{th}(MPa$\sqrt{m}$)	m	FS(MPa)	FS/UTS
AS∥	270.1±10	325±20	4.4±0.7	46.7	1.1	3.1	60	0.22
AS⊥	274.8±8	296.1±20	2.2±0.3	37.9	1.4	3.7	_	_
HS∥	153.4±5	228±13	5.3±0.7	21.7	2.0	3.1	110	0.41
HS⊥	150.3±17	210.1±20	4.2±0.3	19.3	3.1	3.7	_	_
CS∥	262.4±17	330.7±15	3.9±0.6	47.0	1.3	3.4	70	0.22
CS⊥	276.6±15	302.7±15	2.3±0.3	34.5	1.3	3.9	_	_
CC	104.2±11	192.3±15	9±0.5	11.1	3.4	5.4	94.5	0.49

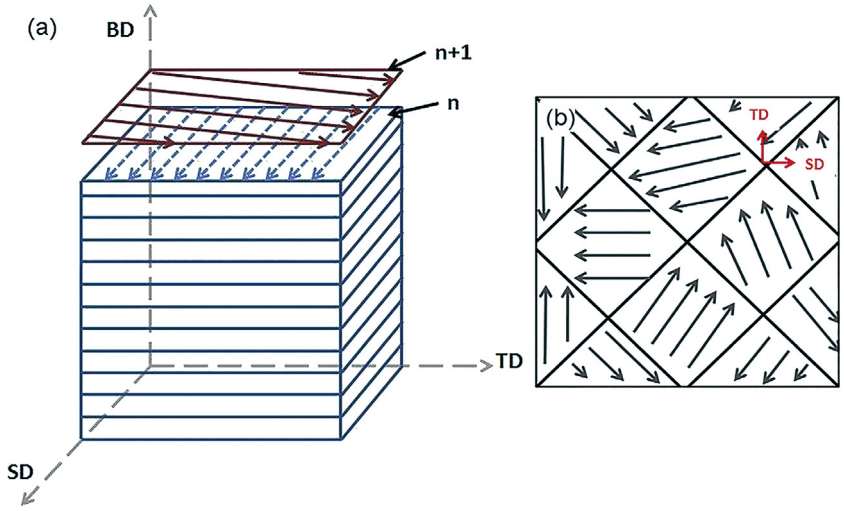

Fig. 13. Schematic diagram of scanning strategy [124]: (a) unidirectional scanning strategy. (b) checkerboard scanning strategy.

The directional solidification of SLM leads to preferential growth in the <100> direction, and the resultant intense texture in the alloy leads to anisotropy [35]. By reducing the layer thickness and the scan spacing to increase the amount of remelting of the prior solidified structure, grains are more likely to grow along the build or Z direction, which can reduce the anisotropy of the alloy [35]. The mechanical property characterization and anisotropy of SLMed AlSi12 alloy compared with casting has been comprehensively explored and examined in the literature [118]. Selected mechanical properties of SLMed and cast AlSi12 alloys are shown in Table 3. AS represents the SLMed alloy with the unidirectional scanning strategy as seen in Fig. 13(a). CS represents the SLMed alloy using the checkerboard scanning strategy shown as Fig. 13(b). ∥ and ⊥ represent parallel and vertical processing directions, respectively.

Table 3 shows that SLMed alloys are almost isotropic in yield strength (YS) and ultimate tensile strength (UTS), which agrees with the results found in literature [132,136]. However, e_f in the ∥ direction is apparently higher than that in the ⊥ direction. The toughness of the SLMed alloy is anisotropic, which is mainly related to the plastic deformation occurring in the microstructure. First, plasticity will cause strain localization, debonding and cavity nucleation at the interface of α-Al/Si [124]. Upon further strain, coalescence of these micropores results in crack formation and fracture. Because of the existence of the coarse Si phase in the heat affected zone, cracks are commonly formed along the laser track. Therefore, the relative orientation between the scanning direction and the loading direction has a great influence on the toughness of the specimen. In addition, as shown in Fig. 14, the laser tracks in the ∥ direction are more tortuous than those in the ⊥ direction [147], which results in higher e_f, K_q and UTS values. Unmelted powder particles due to oxidation and micropores are the main cause of the cracking of specimens [148,149]. Although the ductility is low, the presence of molten pool boundaries enhances the tortuosity of the crack paths and leads to significant crack deflection, which reduces the driving force on the crack tip, thereby increasing the toughness of the alloy [150]. Therefore, the SLM process can increase the strength and toughness of aluminum alloy simultaneously.

The fatigue crack propagation of a specimen follows the Paris law:

$$da/dN = c(\Delta K)^m \quad (2)$$

where c and m are material constants, N is the cycle number of alternating stresses, a is the crack length, and (da/dN) is called the fatigue crack growth rate. The above parameters are listed in Table 3. Due to the low strength of CC, the circular plastic zone ahead of the crack tip is larger, which accelerates crack closure and reduces the driving force of crack growth. Therefore, ΔK_{th} is larger. The higher m value of CC compared with the SLMed alloys is due to the presence of coarse Si dendrites in the microstructure. Fracture and debonding in the circular plastic zone ahead of the crack tip enhance the crack growth rate of each fatigue cycle. Higher ΔK_{th} and m values of the cast specimens indicate higher fatigue crack initiation resistance, but a crack will grow rapidly once it is initiated [151]. For unnotched fatigue properties, the FS/UTS ratio for CC is relative high. The lower FS of SLMed alloys may be due to high tensile residual stresses and unmelted powder particles or pores in the microstructure. Crack initiation always starts at defects (the unmelted powder and pores) due to stress conditions and the local plastic deformation caused by surface discontinuities [152–154]. Pore formation reduces the effective bearing area perpendicular to the layer (Z direction) and causes stress concentrations (notch effect), which lead to a decrease in the static and dynamic strength in the Z direction [142].

3.1.3. *Effect of heat treatment on the microstructure and properties of SLMed Al-Si alloy*

Li et al. [118] has investigated the effect of the heat treatment time on the microstructure and mechanical properties of Al-Si alloys. After heat treatment, the alloy microstructure is trans-

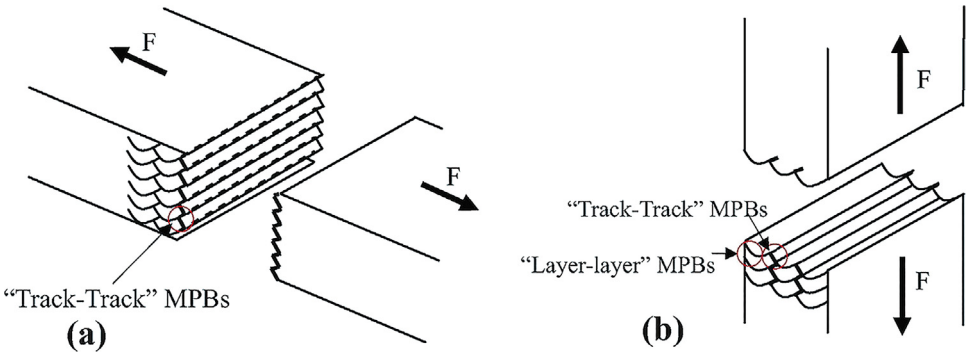

Fig. 14. Possible crack propagation tracks of SLM specimens [147]. (a) ∥ direction. (b) ⊥direction.

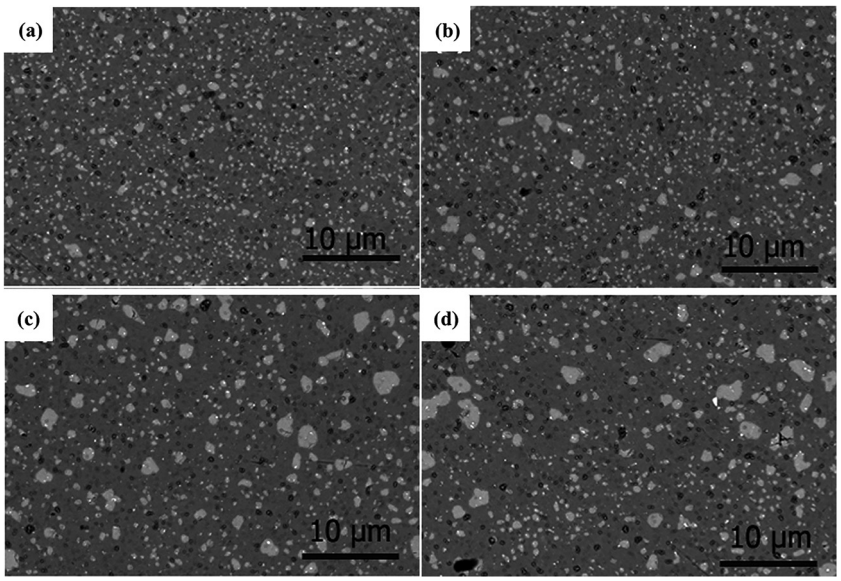

Fig. 15. Microstructure of Al-Si12 after heat treatment [118]. (a) 15 min, (b) 30 min, (c) 2 h, (d) 4 h.

formed from α-Al with a Si network into coarse Si particles uniformly distributed in the Al matrix. As the heat treatment time increases, fine Si particles are precipitated from the supersaturated Al matrix and are deposited on the surface of larger particles. Due to the Ostwald ripening and coalescence of adjacent small Si particles, continued growth of the Si particles occurs. The amount and particle size of eutectic Si increase, but the number of eutectic Si particles decreases, and the difference between a fine grain zone and a coarse grain zone is less obvious, as shown in Fig. 15. The heat treatment temperature has a similar effect in that a higher temperature induces a coarser microstructure and a larger size but smaller number of Si particles [138].

The morphology of the eutectic Si phase plays a significant role in the mechanical properties of AlSi12 alloys. In addition to the interface energy $\gamma^{(Al/Si)}$ between Al and Si, other kinetic or thermodynamic factors, such as the wettability (contact angle θ) and the local concentration of Al and Si atoms, are also of importance to the solidification eutectic microstructure [155–157]. The Si-rich and Al-rich regions in the melt are mostly retained during rapid cooling, and their growth during the cooling process is greatly limited. There is an orientational relationship between Al and Si of (111) Si ∥ (200) Al [118]. When heat treatment is carried out at a high temperature, the Si phase undergoes thermally activated growth; thus, the Si phase can grow along the stable close-packed plane {111}, and the precipitated Si phase is spherical. Compared with the Si phase in flake- or rod-like or acicular shape manufactured by the conventional casting method, the spherical Si particles can reduce the local shear and restrain crack initiation and propagation when deformed. An increase of the Si particle size and a decrease of the number of Si particles reduce the local stress and strain during tensile loading. The residual stress level is also greatly reduced after heat treatment, so the tensile plasticity of the samples is enhanced. As shown in Table 3, the elongation rate reported in the literature [118] reaches 25%.

The mechanical properties of AlSi12 after heat treatment are shown in Table 3. HS represents the alloy processed by SLM with unidirectional scanning and subsequent heat treatment (300 °C, 6 h). From Table 3, it is seen that after heat treatment, YS and UTS decrease remarkably but remain at approximately twice the value for CC. The ductility, especially in the vertical direction, increases substantially, which is consistent with the above analysis. After the Si is precipitated from the Al matrix, the influence of the molten pool boundary on crack propagation is reduced, which decreases the toughness of the sample after heat treatment. The reduction of Kq does not lead to a decrease of ΔK_{th}; conversely, it increased by 100% and 200%, respectively, in the ∥ and ⊥ directions. This is mainly due to the decrease of the yield strength after annealing, which results in more obvious crack blunting and promotes crack closure and a rise of ΔK_{th}. For steady-state fatigue crack growth, the size scale of the cyclic crack tip field is much larger than that of the microstructure, so the crack propagation rate (m) is insensitive to the microstructural parameters. As the annealing process

reduces the tensile residual stress produced during processing, FS rises, which is different from the common case that FS has the same trend as YS.

3.2. Other aluminum alloys

Wrought aluminum alloys have a large solidification temperature range, high crack sensitivity and poor formability. As a result, analogous to welding processes, columnar grains and hot tearing cracks are formed under direct laser irradiation.

Al7075 and Al6061 alloys are the most widely used commercial aluminum alloys due to either high strength or medium strength but good machinability. Many attempts have been made to manufacture high-performance crack-free alloys, but cracking and pore formation are extensive during SLM processing [74,102,158]. The strength of 7075 obtained via SLM is only 200 MPa, and the strength is not changed after heat treatment [159]. Bourell [160] has explored the use of an elemental powder feedstock to mitigate crack formation in Al6061. Here, the methodology involves using approximately 98% pure Al powder with either small amounts of Mg and Si or Mg_2Si particles to eliminate the negative effects of elemental Mg in the microstructure. When SLM processed, the solidification is controlled by the pure Al, which results in a microstructure of Al with isolated particles of Mg and Si (or Mg_2Si). The 6061 microstructure is restored during a post-build homogenization heat treatment, similar to the solutionizing heat treatment of conventionally processed Al6061. Si additions can help improve melt flowability, reduce the thermal expansion coefficient and decrease the eutectic temperature and temperature range of solidification. The addition of Si to the original powder can remarkably increase the density of the samples, but tensile properties are not reported [160,161]. HRL Laboratories [162] demonstrated that crack formation can be resolved by introducing nanoparticles of nucleants that control solidification during laser additive manufacturing. They indicated that solidification shrinkage of interdendritic fluid trapped between the cellular or dendritic grains produced cavities and hot tearing cracks. Equiaxed grains could reduce the effect of trapped liquid, as the grains behaved as a low-resistance granular solid. Based on the crystallographic theories, hydrogen-stabilized Zr nucleants were chosen to coat pre-alloyed gas-atomized 7075 and 6061 spherical powders via an electrostatic assembly technique. In situ synthesized fine Al_3Zr particles provided a large number of ideal low-energy heterogeneous nucleation sites and induced equiaxed microstructures, which easily accommodate the thermal contraction strains associated with solidification, resulting in an alloy system that is highly tear resistant. Finally, the mechanical properties of additively manufactured 7075 are within the expected bounds for wrought counterparts. This metallurgical approach offers a good reference for other crack-susceptible alloys.

By optimizing the processing of 2XXX series Al-Cu-Mg alloy, Zhang et al. [163] found that a dense sample (99.8%) could be obtained using the laser energy density threshold value of 340 J/mm^3. Cu-rich intermetallic compounds are homogeneously distributed in the Al matrix and become coarser at the boundary of the molten pool. The ultimate tensile strength and yield strength are 402 MPa and 276 MPa, respectively. Heat treatment has a remarkable influence on the mechanical properties of SLMed Al-Cu-Mg alloy [164]. When the heat treatment temperature rises from 480°C to 540°C, the microstructure becomes coarser but more homogeneous, as shown in Fig. 16(c). With the increase of the heat treatment solutionizing temperature, UTS, YS and elongation increase by approximately 15%, 22% and 47%, respectively, which is attributed to precipitation strengthening of the S phase (Al_2CuMg). When the temperature is further increased to 560°C, the tensile properties decrease. Because of the low degree of saturation after slow quenching, the size and distribution of the precipitates are no longer helpful for strengthening [165]. Thus, compared with water quenching, UTS, YS and elongation are reduced by 70%, 65% and 56%, respectively, when using air cooling. Under the optimum heat treatment regime (540 °C, 1 h, water quenched), UTS, YS and elongation are 532 MPa, 338 MPa and 13%, respectively. To reduce microcracking and improve the mechanical properties of the alloy, 2 wt% Zr powder was added to the Al-Cu-Mg powder [166]. The addition of Zr leads to the formation of more low melting point phases, which can backfill cracks in the final stage of solidification and reduce crack susceptibility [167]. Al_3Zr particles make the grains change from columnar crystals to ultrafine equiaxed grains (Fig. 16(a), (b) and (d)). The fine grains increase the total grain boundary area per

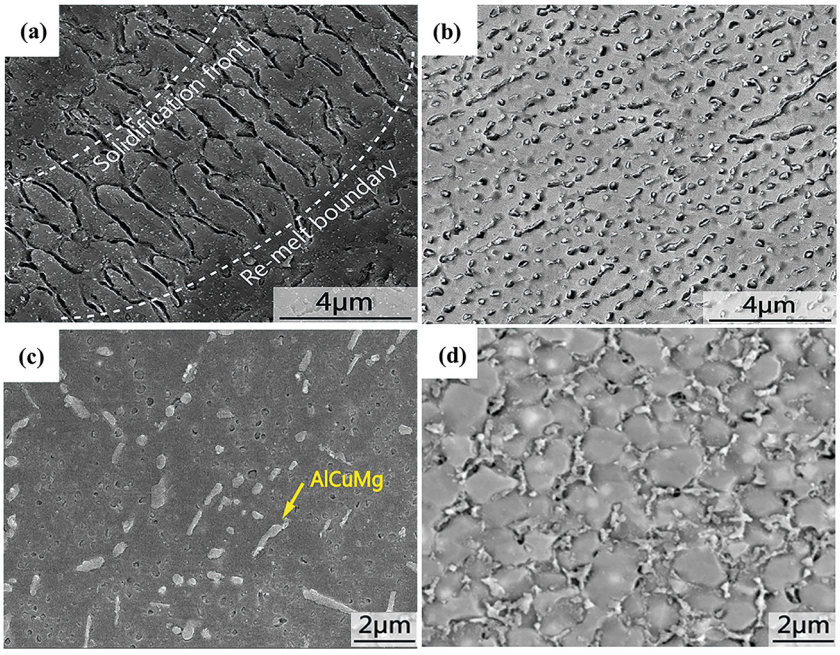

Fig. 16. SEM images of Al–Cu–Mg samples. (a) and (b) SLMed Al–Cu–Mg samples [163]. (c) Al-Cu-Mg alloy after heat treatment [164]. (d) SLMed Zr/Al-Cu-Mg alloy [166].

unit volume, which strengthens the material and suppresses intergranular crack formation [168]. Moreover, with the addition of Zr, the boundary misorientation distribution shifts from a low angle to a high angle, and the distribution nicely follows the ideal distribution for random orientation, which shows that the Zr/Al-Cu-Mg sample fabricated by SLM has low anisotropy. Finally, no obvious microcracking was observed in the specimens, and the yield strength increased to 446 ± 4.3 MPa due to the combined effect of fine grain strengthening and precipitation strengthening. The ultimate strength increased to 451 ± 3.6 MPa.

The type of SLM equipment used for processing can also affect defect formation. Studies at the Universities of Nottingham and Erlangen have shown suppression of crack formation in wrought Al alloys when a Renishaw fabricator is used. This is attributed to a high energy density and a small melt pool. In this regard, the "AM-processability" of the alloys is similar to their weldability, for which certain welding processes are successful and others are not.

4. Prospective

To summarize, the present development obstacles for laser selective melting manufacturing of aluminum alloys mainly include four aspects: the aluminum alloy types suitable for SLM are few, the technological conditions are immature, metallurgical defects are difficult to control and performance studies have not been systematic.

At present, the research studies on aluminum alloy SLM manufacturing have mostly been developed around the influence of the technological parameters and the heat treatment process on the microstructure and mechanical properties of Al-Si alloys. Except for the studies on the 2XXX series Al-Cu-Mg alloy [163,164,166], Al7075 and Al6061 [162], investigations of other casting and wrought aluminum alloys, especially the high strength and heat-resistant aluminum alloys that are in great demand in the aerospace field, have not been reported in detail. In addition, most aluminum alloys manufactured by SLM are at present based on the alloying composition of commercial grades. Non-equilibrium solidification occurring during the SLM process, however, leads to a significantly enhanced solid solution limit of the alloy elements in the matrix metal, which makes it difficult to achieve the desired properties according to the composition of the traditional grades. Therefore, there is a need to broaden the scope of the applicable aluminum alloy types for SLM and design new materials whose composition is suitable for the process characteristics of laser additive manufacturing.

A high level of residual stress and metallurgical defects, such as balling, pores and cracks, commonly occur in SLM-fabricated aluminum alloys, which not only reduces the surface roughness and dimensional accuracy but also results in poor mechanical properties of the components. However, understanding of the formation mechanism of the above defects is still incomplete. The methods of improving SLM technology mainly focus on process parameter adjustment, substrate preheating, laser remelting and scanning strategy variation. Few systematic studies have been conducted to improve part quality via dual-laser online annealing and multi-laser scanning. Moreover, the above improvements are mostly from the viewpoint of technology. The scientific characterization of these methods has not been explained and analyzed in detail. Theoretical computer simulations and experiments are needed to advance our understanding and to improve part quality.

Because of the directionality of laser scanning, components tend to show some degree of anisotropy. Thus far, most research on the performance of SLMed aluminum alloys has focused on the mechanical properties, especially the tensile properties. Relatively few studies have been conducted on the fracture and fatigue properties. Aluminum alloys also have excellent thermal and electrical properties. Research on these comprehensive properties and on the anisotropy of SLMed aluminum alloys will be important in the future. On the other hand, the manufacturing flexibility of the SLM process can be realized by incorporating lattice and porous structures and other complex part geometries. Since SLM technology is interdisciplinary in nature, it is meaningful to combine the advantages of SLM with mechanical and structural design to realize a complete process from the design to the manufacturing of complete structures or functional components.

Acknowledgements

This work was sponsored by National Key Research and Development Program "Additive Manufacturing and Laser Manufacturing" (No. 2016YFB1100101), Natural and Science Foundation of China (Grant Nos. 51775208, 51505166), Hubei Science Fund for Distinguished Young Scholars (No. 0216110085), Wuhan Morning Light Plan of Youth Science and Technology (No. 0216110066), Graduates' Innovation Fund, Huazhong University of Science and Technology (No. 5003110027), Fundamental Research Funds for the Central University (No. 2017JYCXJJ004), and the Academic frontier youth team at Huazhong University of Science and Technology (HUST).

References

[1] J.C. Williams, E.A.S. Jr, Acta Mater. 51 (2003) 5775–5799.
[2] A. Heinz, A. Haszler, C. Keidel, S. Moldenhauer, R. Benedictus, W.S. Miller, Mater. Sci. Eng. A 280 (2000) 102–107.
[3] W. Xu, Y. Luo, Wei. Zhang, M. Fu, J. Mater. Sci. Technol. 34 (2018) 173–184.
[4] C. Kammer, Aluminium Handbook, Aluminium-Verlag Marketing & Kommunikation GmbH, Germany, 1999, pp. 61–73.
[5] E.A.S. Jr, J.T. Staley, Prog. Aerosp. Sci. 32 (1996) 131–172.
[6] S. Fu, Y. Zhang, H. Liu, D. Yi, B. Wang, Y. Jiang, Z. Chen, N. Qi, J. Mater. Sci. Technol. 34 (2018) 335–343.
[7] C. Cui, Y. Shen, F. Meng, J. Mater. Sci. Technol. 16 (2000) 619–626.
[8] S. Ranganath, J. Mater. Sci. Technol. 32 (1997) 1–16.
[9] S.C. Tjong, Z.Y. Ma, Mater. Sci. Eng. R 29 (2000) 49–113.
[10] L. He, J. Kang, T. Huang, K. Rong, Heat Treat. Met. 31 (2004) 69–72.
[11] W. Li, K. Yang, S. Yin, X. Yang, Y. Xu, R. Lupoi, J. Mater. Sci. Technol. 34 (2018) 440–457.
[12] R.S. Mishra, Z.Y. Ma, Mater. Sci. Eng. R 50 (2005) 1–78.
[13] F. Nie, H. Dong, S. Chen, P. Li, L. Wang, Z. Zhao, X. Li, H. Zhang, J. Mater. Sci. Technol. 34 (2018) 551–560.
[14] Y. Liu, Y. Yang, S. Mai, D. Wang, C. Song, Mater. Des. 87 (2015) 797–806.
[15] J.P. Kruth, L. Froyen, J.V. Vaerenbergh, P. Mercelis, M. Rombouts, B. Lauwers, J. Mater. Process. Tech. 149 (2004) 616–622.
[16] J.P. Kruth, G. Levy, F. Klocke, T.H.C. Childs, CIRP Ann. Manuf. Tech. 56 (2007) 730–759.
[17] L.E. Murr, S.M. Gaytan, D.A. Ramirez, E. Martinez, J. Hernandez, K.N. Amato, P.W. Shindo, F.R. Medina, R.B. Wicker, J. Mater. Sci. Technol. 28 (2012) 1–14.
[18] N. Contuzzi, S.L. Campanelli, A.D. Ludovico, Int. J. Simul. Model 10 (2011) 113–121.
[19] S.L. Sing, J. An, W.Y. Yeong, F.E. Wiria, J. Orthop. Res. 34 (2016) 369–385.
[20] D. Gu, P. Yuan, J. Appl. Phys. 118 (2016) 401–477.
[21] S. Pauly, L. Löber, R. Petters, M. Stoica, S. Scudino, U. Kühn, J. Eckert, Mater. Today 16 (2013) 37–41.
[22] Y. Zhang, J. Zhang, Q. Yan, L. Zhang, M. Wang, B. Song, Y. Shi, Scripta Mater. 148 (2018) 20–23.
[23] K.G. Prashanth, J. Eckert, J. Alloy Compd. 707 (2016) 27–34.
[24] Y. Yang, J. Liu, Z. Luo, D. Wang, Rapid Prototyp. J. 18 (2012) 482–489.
[25] B. Song, S. Dong, P. Coddet, H. Liao, C. Coddet, Mater. Des. 53 (2014) 1–7.
[26] P. Chalker, A. Clare, S. Davies, C.J. Sutcliffe, S. Tsopanos, Int. J. Mech. Mater. Des. 4 (2008) 181–187.
[27] G. Levy, N. Herres, A.B. Spierings, D. Bourell, Rapid Prototyp. J. 17 (2010) 195–202.
[28] Q. Shi, D. Gu, M. Xia, S. Cao, T. Rong, Opt. Laser Technol. 84 (2016) 9–22.
[29] D. Gu, W. Meiners, K. Wissenbach, R. Poprawe, Int. Mater. Rev. 57 (2012) 133–164.
[30] M. Peel, A. Steuwer, M. Preuss, P.J. Withers, Acta Mater. 51 (2003) 4791–4801.
[31] C.V. Robino, J.R. Michael, M.C. Maguire, Weld. J. 77 (1998) 446S–457S.
[32] T.W. Nelson, J.C. Lippold, M.J. Mills, Weld. J. 78 (1999) 329S–337S.
[33] C. Wang, J. Zhang, L. Liu, H. Fu, J. Mater. Sci. Technol. 27 (2011) 668–672.
[34] M. Gäumann, S. Henry, F. Cléton, J.D. Wagnière, W. Kurz, Mater. Sci. Eng. A 271 (1999) 232–241.

[35] L. Thijs, K. Kempen, J.P. Kruth, J.V. Humbeeck, Acta Mater. 61 (2013) 1809–1819.
[36] S. Wu, Y. Liu, Principle of Materials Forming, China Machine Press, Beijing, 2008, pp. 123–154 (in Chinese).
[37] G. Çam, S. Mistikoglu, J. Mater. Eng. Perform. 23 (2014) 1936–1953.
[38] W. Huang, C. Chuang, C. Lin, C. Wu, D. Lin, S. Liu, W. Tseng, J. Horng, Phys. Procedia 56 (2014) 58–63.
[39] H. Fu, J. Mater. Sci. Technol. 17 (2001) 299–302.
[40] H. Yamagata, W. Kasprzak, M. Aniolek, H. Kurita, J.H. Sokolowski, J. Mater. Process. Tech. 203 (2008) 333–341.
[41] S. Guo, Solidification Behavior of Spray Deposited Al-Zn-Mg-Cu Alloys and Their Microstructural Evolution During Thermal Processing, Ph.D. Thesis, Harbin Institute of Technology, 2011 (in Chinese).
[42] X. Xu, Y. Zhao, H. Hou, F. Liu, J. Alloy Compd. 744 (2018) 740–749.
[43] Q. Zhang, H. Xue, Q. Tang, S. Pan, M. Rettenmayr, M. Zhu, Comp. Mater. Sci. 146 (2018) 204–212.
[44] S. Liu, H. Zhu, G. Peng, J. Yin, X. Zeng, Mater. Des. 142 (2018) 319–328.
[45] Y. Liu, Z. Liu, Y. Jiang, G. Wang, Y. Yang, L. Zhang, J. Alloy Compd. 735 (2018) 1414–1421.
[46] P. Sharifi, J. Jamali, K. Sadayappan, J.T. Wood, J. Mater. Process. Tech. 34 (2018) 324–334.
[47] D. Bourell, H.L. Marcus, J.W. Barlow, J.J. Beaman, Int. J. Powder Met. 28 (1992) 369–381.
[48] R. Li, Research on the Key Basic Issues in Selective Laser Melting of Matallic Powder, Ph.D. Thesis, Huazhong University of Science and Technology, 2010 (in Chinese).
[49] C.Y. Yap, C.K. Chua, Z. Dong, Z. Liu, D. Zhang, L.E. Loh, S.L. Sing, Appl. Phys. Rev. 2 (2015), 518-187.
[50] W. Wu, Y. Yang, D. Wang, J. South China Univ. Techno. Nat. Sci. Ed. 38 (2010) 110–115 (in Chinese).
[51] X. Zhang, X. Liu, D. Zhang, Z. Shen, W. Liu, J. Mater. Process. Tech. 222 (2015) 33–42.
[52] M. Shiomi, K. Osakada, K. Nakamura, T. Yamashita, F. Abe, CIRP Ann. Manuf. Techn. 53 (2004) 195–198.
[53] X. Shi, S. Ma, C. Liu, Q. Wu, Opt. Laser Technol. 90 (2017) 71–79.
[54] J. Yang, J. Han, H. Yu, J. Yin, M. Gao, Z. Wang, X. Zeng, Mater. Des. 110 (2016) 558–570.
[55] E. Yasa, J.P. Kruth, J. Deckers, CIRP Ann. Manuf. Techn. 60 (2011) 263–266.
[56] E. Yasa, J.P. Kruth, Procedia Eng. 19 (2011) 389–395.
[57] B. Song, S. Dong, H. Liao, C. Coddet, Mater. Res. Innov. 16 (2012) 321–325.
[58] I. Yadroitsev, P. Krakhmalev, I. Yadroitsava, S. Johansson, I. Smurov, J. Mater. Process. Tech. 213 (2013) 606–613.
[59] D. Gu, Y.C. Hagedorn, W. Meiners, G. Meng, R.J.S. Batista, K. Wissenbach, R. Poprawe, Acta Mater. 60 (2012) 3849–3860.
[60] Q. Jia, D. Gu, J. Alloy Compd. 585 (2014) 713–721.
[61] D. Dai, D. Gu, Mater. Des. 55 (2014) 482–491.
[62] R. Xiao, X. Zhang, J. Manuf. Process. 16 (2014) 166–175.
[63] M. Xia, D. Gu, G. Yu, D. Dai, H. Chen, Q. Shi, Int. J. Mach. Tool Manu. 116 (2017) 96–106.
[64] K. Monroy, J. Delgado, J. Ciurana, Procedia Eng. 63 (2013) 361–369.
[65] P.A. Kobryn, E.H. Moore, S.L. Semiatin, Scr. Mater. 43 (2000) 299–305.
[66] M. Ma, Z. Wang, M. Gao, X. Zeng, J. Mater, Process. Tech. 215 (2015) 142–150.
[67] E.O. Olakanmi, R.F. Cochrane, K.W. Dalgarno, J. Mater. Process. Tech. 211 (2011) 113–121.
[68] N.T. Aboulkhair, N.M. Everitt, I. Ashcroft, C. Tuck, Addit. Manuf. s1-4 (2014) 77–86.
[69] Y. Fu, N. Kang, H. Liao, Y. Gao, C. Coddet, Intermetallics 86 (2017) 51–58.
[70] W.E. King, H.D. Barth, V.M. Castillo, G.F. Gallegos, J.W. Gibbs, D.E. Hahn, C. Kamath, A.M. Rubenchik, J. Mater. Process. Tech. 214 (2014) 2915–2925.
[71] D. Dai, D. Gu, Appl. Surf. Sci. 355 (2015) 310–319.
[72] X. Wang, L. Zhang, M. Fang, T.B. Sercombe, Mater. Sci. Eng. A 597 (2014) 370–375.
[73] X. Cao, W. Wallace, C. Poon, J.P. Immarigeon, Mater. Manuf. Prog. 18 (2003) 23–49.
[74] N. Kaufmann, M. Imran, T.M. Wischeropp, C. Emmelmann, S. Siddique, F. Walther, Phys. Procedia 83 (2016) 918–926.
[75] A. Hussein, L. Hao, C. Yan, R. Everson, Mater. Des. 52 (2013) 638–647.
[76] C. Li, C. Fu, Y. Guo, F. Fang, J. Mater. Process. Tech. 229 (2016) 703–712.
[77] G. Çam, Int. Mater. Rev. 56 (2014) 1–48.
[78] C.M. Chen, R. Kovacevic, Int. J. Mach. Tool Manu. 43 (2003) 1319–1326.
[79] D. Deng, H. Murakawa, Mater. Sci. 37 (2006) 269–277.
[80] P. Mercelis, J.P. Kruth, Rapid Prototyp. J. 12 (2006) 254–265.
[81] D. Kim, J. Hwang, E. Kim, Y. Heo, W. Woo, S.H. Choi, J. Alloy Compd. 714 (2017) 687–697.
[82] L.E. Lindgren, Comput. Method Appl. M. 195 (2006) 6710–6736.
[83] D. Ouyang, N. Li, W. Xing, J. Zhang, L. Liu, Intermetallics 90 (2017) 128–134.
[84] E.O. Olakanmi, R.F. Cochrane, K.W. Dalgarno, Prog. Mater. Sci. 74 (2015) 401–477.
[85] C. Huang, S. Kou, Weld. J. 84 (2004) 63s–71s.
[86] Y. Chen, K. Zhang, J. Huang, S.R.E. Hosseini, Z. Li, Mater. Des. 90 (2016) 586–594.
[87] D.G. Eskin, L. Suyitno, Katgerman, Prog. Mater. Sci. 49 (2004) 629–711.
[88] J.H. Dudas, Weld. J. 45 (1966).
[89] R. Liu, Z. Dong, Y. Pan, Chin. J. Nonferrous Met. 16 (2006) 110–116 (in Chinese).
[90] L.N. Carter, C. Martin, P.J. Withers, M.M. Attallah, J. Alloy Compd. 615 (2014) 338–347.
[91] M.G. Collins, J.C. Lippold, Weld. J. 83 (2003), 39/S-49/S.
[92] M.G. Collins, A.J. Ramirez, J.C. Lippold, Weld. J. 83 (2003), 39/S-49/S.
[93] N. Coniglio, C.E. Cross, Int. Mater. Rev. 58 (2013) 375–397.
[94] P.V. Witzendorff, S. Kaierle, O. Suttmann, L. Overmeyer, Metall. Mater. Trans. A 46 (2015) 1678–1688.
[95] L. Thijs, F. Verhaeghe, T. Craeghs, J.V. Humbeeck, J.P. Kruth, Acta Mater. 58 (2010) 3303–3312.
[96] H. Zhao, D.R. White, T. Debroy, Int. Mater. Rev. 44 (1999) 238–266.
[97] D. Choo, H. Moon, T. Kang, S. Lee, Mater. Trans. A 32 (2001) 2249–2258.
[98] Y. Liu, Y. Yang, D. Wang, Int. J. Adv. Manuf. Tech. 87 (2016) 647–656.
[99] A. Jalar, N.A.C. Lah, N.K. Othman, R. Shamsudin, A.R. Daud, S.R.S. Bakar, Adv. Mater. Sci. Eng. 2014 (2015) 1–10.
[100] M. Simonelli, C. Tuck, N.T. Aboulkhair, I. Maskery, I. Ashcroft, R.D. Wildman, R. Hague, Metall. Mater. Trans. A 46 (2015) 3842–3851.
[101] Q. Jia, D. Gu, Opt. Laser Technol. 62 (2014) 161–171.
[102] E. Louvis, P. Fox, C.J. Sutcliffe, J. Mater, Progress. Tech. 211 (2011) 275–284.
[103] C. Weingarten, D. Buchbinder, N. Pirch, W. Meiners, K. Wissenbach, R. Poprawe, J. Mater, Process. Tech. 221 (2015) 112–120.
[104] A. Klassen, V.E. Forster, C. Körner,Modell. Simul. Mater. Sci. Eng. 25 (2016), 025033.
[105] A. Klassen, V.E. Forster, V. Juechter, C. Körner, J. Mater. Process. Tech. 247 (2017) 280–288.
[106] C. Panwisawas, C. Qiu, M.J. Anderson, Y. Sovani, R.P. Turner, M.M. Attallah, J.W. Brooks, H.C. Basoalto, Comp. Mater. Sci. 126 (2017) 479–490.
[107] Z. Mao, D. Zhang, P. Wei, K. Zhang, Materials 10 (2017) 333.
[108] M. Pastor, H. Zhao, R.P. Martukanitz, T. Debroy, Weld. J. 78 (1999) 207s–216s.
[109] M. Rombouts, J.P. Kruth, L. Froyen, P. Mercelis, CIRP Ann. Manuf. Technol. 55 (2006) 187–192.
[110] H. Shipley, D. Mcdonnell, M. Culleton, R. Lupoi, G. O'Donnell, D. Trimble, Int. J. Mach. Tool Manu. 128 (2018) 1–20.
[111] I. Yadroitsev, A. Gusarov, I. Yadroitsava, I. Smurov, J. Mater. Process. Tech. 210 (2010) 1624–1631.
[112] E.O. Olakanmi, J. Mater. Process. Tech. 213 (2013) 1387–1405.
[113] C.C. Ng, M.M. Savalani, M.L. Lau, H.C. Man, Appl. Surf. Sci. 257 (2011) 7447–7454.
[114] X. Wang, Process Parameters and Properties of Selective Laser Melting Al-Si Alloys, Ph.D. Thesis, China University of Geosciences (Beijing), Beijing, 2014 (in Chinese).
[115] H. Ye, J. Mater. Eng. Perform. 12 (2003) 288–297.
[116] Q. Wang, C.J. Davidson, J. Mater. Sci. 26 (2001) 739–750.
[117] W. Li, S. Li, J. Liu, A. Zhang, Y. Zhou, Q. Wei, C. Yan, Y. Shi, Mater. Sci. Eng. A 663 (2016) 116–125.
[118] X. Li, X. Wang, M. Saunders, A. Suvorova, L. Zhang, Y. Liu, M. Fang, Z. Huang, T.B. Sercombe, Acta Mater. 95 (2015) 74–82.
[119] M. Calvo-Dahlborg, P.S. Popel, M.J. Kramer, M. Besser, J.R. Morris, U. Dahlborg, J. Alloy Compd. 550 (2013) 9–22.
[120] W. Liu, L. Ye, K. Liu, J. Appl. Phys. 109 (2011), 043109-043109-5.
[121] S.D. Mcdonald, K. Nogita, A.K. Dahle, Acta Mater. 52 (2004) 4273–4280.
[122] M. Gremaud, D.R. Allen, M. Rappaz, J.H. Perepezko, Acta Mater. 44 (1996) 2669–2681.
[123] Y.T. Pei, J.T.M.D. Hosson, Acta Mater. 48 (2000) 2617–2624.
[124] J. Suryawanshi, K.G. Prashanth, S. Scudino, J. Eckert, O. Prakash, U. Ramamurty, Acta Mater. 115 (2016) 285–294.
[125] B. Chen, S.K. Moon, X. Yao, G. Bi, J. Shen, J. Umeda, K. Kondoh, Scripta Mater. 141 (2017) 45–49.
[126] D.A. Lados, D. Apelian, J.K. Donald, Acta Mater. 54 (2006) 1475–1486.
[127] D. Buchbinder, H. Schleifenbaum, S. Heidrich, W. Meiners, J. Bültmann, Phys. Procedia 12 (2011) 271–278.
[128] D. Gu, W. Meiners, Mater. Sci. Eng. A 527 (2010) 7585–7592.
[129] N. Kang, P. Coddet, C. Chen, Y. Wang, H. Liao, C. Coddet, Mater. Des. 99 (2016) 120–126.
[130] N. Kang, P. Coddet, H. Liao, C. Coddet, J. Alloy Compd. 662 (2016) 259–262.
[131] T. Kimura, T. Nakamoto, M. Mizuno, H. Araki, Mater. Sci. Eng. A 682 (2017) 593–602.
[132] N. Read, W. Wang, K. Essa, M.M. Attallah, Mater. Des. 65 (2015) 417–424.
[133] K. Kempen, L. Thijs, J.V. Humbeeck, J.P. Kruth, Mater. Sci. Tech. Lond. 31 (2015) 917–923.
[134] P. Wei, Z. Wei, Z. Chen, J. Du, Y. He, J. Li, Y. Zhou, Appl. Surf. Sci. 408 (2017) 38–50.
[135] N.T. Aboulkhair, I. Maskery, C. Tuck, I. Ashcroft, N.M. Everitt, Mater. Sci. Eng. A 667 (2016) 139–146.
[136] L. Wang, X. Jiang, M. Guo, X. Zhu, B. Yan, Mater. Sci. Tech. Lond 33 (2017) 1–9.
[137] M. Fousová, D. Dvorský, A. Michalcová, D. Vojtěch, Mater. Charact. 137 (2018) 119–126.
[138] K.G. Prashanth, S. Scudino, H.J. Klauss, K.B. Surreddi, L. Löber, Z. Wang, A.K. Chaubey, U. Kühn, J. Eckert, Mater. Sci. Eng. A 590 (2014) 153–160.
[139] T. Kimura, T. Nakamoto, Mater. Des. 89 (2016) 1294–1301.
[140] Y. Bai, Y. Yang, Z. Xiao, M. Zhang, D. Wang, Mater. Des. 140 (2018) 257–266.
[141] F. Trevisan, F. Calignano, M. Lorusso, J. Pakkanen, A. Aversa, E.P. Ambrosio, M. Lombardi, P. Fino, D. Manfredi, Materials 10 (2017) 1–23.
[142] E. Brandl, U. Heckenberger, V. Holzinger, D. Buchbinder, Mater. Des. 34 (2012) 159–169.
[143] S. Siddique, M. Imran, F. Walther, Int. J. Fatigue 94 (2016) 246–254.

[144] S. Leuders, M. Vollmer, F. Brenne, T. Tröster, T. Niendorf, Metall. Mater. Trans. A 46 (2015) 3816–3823.
[145] A. Riemer, S. Leaders, H.A. Richard, T. Tröster, Materialprufung 55 (2013) 537–543.
[146] A. Riemer, S. Leuders, M. Thöne, H.A. Richard, T. Tröster, T. Niendorf, Eng. Fract. Mech. 120 (2014) 15–25.
[147] S. Wen, S. Li, Q. Wei, C. Yan, S. Zhang, Y. Shi, J. Mater. Process. Tech. 214 (2014) 2660–2667.
[148] Z. Wang, K. Guan, M. Gao, X. Li, X. Chen, X. Zeng, J. Alloy Compd. 513 (2012) 518–523.
[149] H. Gong, K. Rafi, H. Gu, G.D.J. Ram, T. Starr, B. Stucker, Mater. Des. 86 (2015) 545–554.
[150] R.I. Stephens, A. Fatemi, R.R. Stephens, H.O. Fuchs, J. Mater. Sci. Technol. 103 (1981) 415–432.
[151] S. Suresh, Fatigue Fract. Eng. M. 28 (1998) 1153–1160.
[152] H.R. Ammar, A.M. Samuel, F.H. Samuel, Int. J. Fatigue 30 (2008) 1024–1035.
[153] G. Qian, Y. Hong, C. Zhou, Eng. Fail. Anal. 17 (2010) 1517–1525.
[154] A. Leon, E. Aghion, Mater. Charact. 131 (2017) 188–194.
[155] D. Qiu, M. Zhang, J. Alloy Compd. 586 (2014) 39–44.
[156] S. Hegde, K.N. Prabhu, J. Mater. Sci. 43 (2008) 3009–3027.
[157] M. Asta, C. Beckermann, A. Karma, W. Kurz, R. Napolitano, M. Plapp, G. Purdy, M. Rappaz, R. Trivedi, Acta Mater. 57 (2009) 941–971.
[158] P. Wang, H. Li, K.G. Prashanth, J. Eckert, S. Scudino, J. Alloy Compd. 707 (2016) 287–290.
[159] W. Reschetnik, J.P. Brüggemann, M.E. Aydinöz, O. Grydin, K.P. Hoyer, G. Kullmer, H.A. Richard, Procedia Struct. Integr. 2 (2016) 3040–3048.
[160] C.E. Roberts, D. Bourell, T. Watt, J. Cohen, Phys. Procedia 83 (2016) 909–917.
[161] M.L.M. Sistiaga, R. Mertens, B. Vrancken, X. Wang, B.V. Hooreweder, J.P. Kruth, J.V. Humbeeck, J. Mater. Process. Tech. 238 (2016) 437–445.
[162] J.H. Martin, B.D. Yahata, J.M. Hundley, J.A. Mayer, T.A. Schaedler, T.M. Pollock, Nature 549 (2017) 365.
[163] H. Zhang, H. Zhu, T. Qi, Z. Hu, X. Zeng, Mater. Sci. Eng. A 656 (2016) 47–54.
[164] H. Zhang, H. Zhu, X. Nie, T. Qi, Z. Hu, X. Zeng, in: B. Gu, H. Helvajian, A. Pique (Eds.), Fabrication and Heat Treatment of High Strength Al-Cu-Mg Alloy Processed Using Selective Laser Melting, E-Publishing, Inc., San Francisco, 2016, pp. 97380X1-97380X7.
[165] E.M. Elgallad, P. Shen, Z. Zhang, X. Chen, Mater. Des. 61 (2014) 133–140.
[166] H. Zhang, H. Zhu, X. Nie, J. Yin, Z. Hu, X. Zeng, Scripta Mater. 134 (2017) 6–10.
[167] F.M. Ghaini, M. Sheikhi, M.J. Torkamany, J. Sabbaghzadeh, Mater. Sci. Eng. A 519 (2009) 167–171.
[168] E.A. Jägle, Z. Sheng, L. Wu, L. Lu, J. Risse, A. Weishelt, D. Raabe, JOM-US 68 (2016) 943–949.